

1 **Phase partitioning and volatility of secondary organic aerosol**
2 **components formed from α -pinene ozonolysis and OH oxidation: the**
3 **importance of accretion products and other low volatility compounds**

4
5 F. D. Lopez-Hilfiker¹, C. Mohr^{1,7}, M. Ehn^{2,3}, F. Rubach³, E. Kleist⁴, J. Wildt⁴, Th. F.
6 Mentel³, A. J. Carrasquillo⁶, K. E. Daumit⁶, J. F. Hunter⁶, J. H. Kroll⁶, D. R. Worsnop^{2,6}, J.
7 A. Thornton^{1,2,3*}

8
9 ¹ Department of Atmospheric Sciences, University of Washington, Seattle, WA, 98195, USA

10 ² Department of Physics, P.O. Box 64, 00014, University of Helsinki, Helsinki, Finland

11 ³ Institute for Energy and Climate Research (IEK-8), Forschungszentrum Jülich, 52425 Jülich, Germany

12 ⁴ Institute of Bio-Geosciences (IBG-2), Forschungszentrum Jülich, 52425 Jülich, Germany

13 ⁵ Center for Aerosol and Cloud Chemistry, Aerodyne Research, Inc., Billerica, MA, USA

14 ⁶ Department of Civil and Environmental Engineering, Massachusetts Institute of Technology, Cambridge,
15 MA 02139, USA

16 ⁷ Institute for Meteorology and Climate Research, Karlsruhe Institute of Technology, 76344 Eggenstein-
17 Leopoldshafen, Germany

18
19
20 **Abstract.** We measured a large suite of gas and particle phase multi-functional organic
21 compounds with a Filter Inlet for Gases and AEROsols (FIGAERO) coupled to a high-
22 resolution time-of-flight chemical ionization mass spectrometer (HR-ToF-CIMS)
23 developed at the University of Washington. The instrument was deployed on
24 environmental simulation chambers to study monoterpene oxidation as a secondary
25 organic aerosol (SOA) source. We focus here on results from experiments utilizing an
26 ionization method most selective towards acids (acetate negative ion proton transfer), but
27 our conclusions are based on more general physical and chemical properties of the SOA.
28 Hundreds of compounds were observed in both gas and particle phases, the latter being
29 detected upon temperature programmed thermal desorption of collected particles.
30 Particulate organic compounds detected by the FIGAERO HR-ToF-CIMS are highly
31 correlated with, and explain at least 25 – 50% of, the organic aerosol mass measured by
32 an Aerodyne Aerosol Mass Spectrometer (AMS). Reproducible multi-modal structures in
33 the thermograms for individual compounds of a given elemental composition reveal a
34 significant SOA mass contribution from high molecular weight organics and/or oligomers
35 (i.e. multi-phase accretion reaction products). Approximately 50% of the HR-ToF-CIMS
36 particle phase mass is associated with compounds having effective vapor pressures 4 or

37 more orders of magnitude lower than commonly measured monoterpene oxidation
38 products. The relative importance of these accretion-type and other extremely low
39 volatility products appears to vary with photochemical conditions. We present a
40 desorption temperature based framework for apportionment of thermogram signals into
41 volatility bins. The volatility-based apportionment greatly improves agreement between
42 measured and modeled gas-particle partitioning for select major and minor components
43 of the SOA, consistent with thermal decomposition during desorption causing the
44 conversion of lower volatility components into the detected higher volatility compounds.

45

46 **1. Introduction.** The sources, oxidation pathways and chemical properties of secondary
47 organic aerosol (SOA) remain highly uncertain on a molecular basis. These uncertainties
48 can lead to large errors between modeled and measured aerosol loadings (Heald et al.,
49 2010; Volkamer et al., 2006), and ultimately limit our ability to confidently predict
50 changes in aerosol properties under a warming climate (Hallquist et al., 2009) or in
51 response to other anthropogenic perturbations such as emissions of nitrogen oxides and
52 sulfur dioxide. To develop adequate model parameterizations of organic aerosol (OA)
53 formation, growth, and loss, there remains a need to improve and evaluate chemical
54 mechanisms that involve conversion and partitioning of organic compounds between gas
55 and condensed phases (Roldin et al., 2014). These needs are likely to be at least partially
56 addressed by a more detailed understanding of molecular composition in both phases at
57 higher time resolution from which mechanistic insights are more easily discerned.

58

59 While SOA is ubiquitous in the lower atmosphere, our understanding of its composition
60 and properties, from nucleation and growth of freshly formed particles to background
61 ambient particles, is still lacking (Donahue et al., 2011; Ehn et al., 2014; Riccobono et al.,
62 2014; Riipinen et al., 2012; Ziemann, 2002). Identifying the sources and functional
63 groups of organic molecules within SOA remains a difficult analytical challenge, given
64 that their inherent low volatility makes routine online analysis by mass spectrometry
65 impossible without perturbation (thermal desorption, dissolution, derivatization, etc.) and
66 that the actual source molecules initially condensing into the particle phase may have

67 been transformed *via* condensed phase chemistry, such as acid-base reactions or various
68 organic accretion processes (Smith et al., 2010; Ziemann and Atkinson, 2012).

69

70 Recently, *in situ* measurement methods have been developed which can address the
71 volatility distribution or molecular composition of organic aerosol. Volatility Tandem
72 Differential Mobility Analyzers (VTDMA) allow the measurement of kinetic evaporation
73 in a series of ovens, which can be used to constrain the bulk volatility of compounds
74 present in the aerosol (Cappa, 2010). Similarly, thermal denuders have been coupled to
75 aerosol mass spectrometers to examine the loss organic aerosol mass during transit
76 through a programmatically heated oven with some molecular information derived from
77 factor analysis (Cappa and Jimenez, 2010). Other chemically speciated measurements,
78 for example the TAG (Thermal Desorption Aerosol Gas Chromatograph) (Williams et al.,
79 2006) measure the molecular composition of thermally desorbed compounds but lack a
80 direct measure of the aerosol volatility and rather use functional group dependencies to
81 infer the volatility distribution based on detected compositions. Holzinger et al. coupled
82 an analogous collection-thermal-desorption (CTD) inlet to a PTR-MS (Proton Transfer
83 Reaction Mass Spectrometer) to detect organic and inorganic compounds while also
84 providing thermogram information, but this type of chemical ionization often leads to
85 fragmentation and dehydration (Holzinger et al., 2010). We recently developed the
86 FIGAERO (Filter Inlet for Gases and Aerosol), which allows both the separation of
87 components in a volatility space, via a temperature programmed thermal desorption, and
88 determination of the corresponding molecular composition on an hourly timescale
89 (Lopez-Hilfiker et al., 2014).

90

91 We present measurements of compounds produced from α -pinene oxidation by OH and
92 ozone in an environmental simulation chamber using the FIGAERO coupled to a
93 HRToF-CIMS (Lopez-Hilfiker et al., 2014). Carboxylic acids are thought to be important
94 components of monoterpene-derived SOA, in part because the acid functionality
95 represents an approximate end point in carbon oxidation state and its incorporation leads
96 to a significant reduction (1000-fold) in vapor pressure relative to the parent compound
97 (Capouet and Müller, 2006; Russell et al., 2011). We therefore chose acetate negative

98 proton transfer ionization, which is most sensitive to carboxylic acid groups (Veres et al.,
99 2010; 2008), though also detects other functionalities as we have previously
100 demonstrated and extend herein (Mohr et al., 2013). Our main goal is not so much a
101 functional group characterization but to examine the extent to which compounds
102 containing acid functionalities contribute to the SOA and the distribution of these
103 compounds in a volatility/abundance space. We find that a significant fraction of the
104 SOA mass characterized by the HR-ToF-CIMS is of extremely low volatility, 4 or more
105 orders of magnitude lower than typical monoterpene oxidation products. We discuss the
106 implications of these compounds with respect to partitioning models and the lifetime of
107 atmospheric aerosol.

108

109 **2. Experimental Methods.** A prototype FIGAERO-HRToF-CIMS was coupled to both
110 the Jülich Plant Atmosphere Chamber (JPAC, Jülich Forschungszentrum, Germany
111 (Mentel et al., 2009) and a smaller chamber with similar conditions at the University of
112 Washington (UW). Below we provide detailed descriptions of the coupling of the
113 FIGAERO-HRToF-CIMS to the JPAC and UW chambers.

114

115 **2.1 Simulation Chambers.** Most data presented here was obtained at the Jülich Plant
116 Atmosphere Chamber (JPAC) (Mentel et al., 2009), which consists of a series of glass
117 chambers housed in separate temperature controlled rooms. We used a 1450 L
118 borosilicate glass chamber housed in a temperature-controlled room held at 15 °C and
119 relative humidity (RH) of 35 to 65%. The chamber is operated under steady-state
120 conditions and is continuously stirred by a mixer mounted at the top of the chamber. The
121 residence time is on average 50 minutes at a flush rate of ~30 slpm. The chamber is
122 equipped with different types of UV lamps, one set can be used for photolysis of NO₂ to
123 NO and the other set of lamps for OH production from O₃ photolysis in the presence of
124 H₂O. The OH lamps can be shielded such that the actinic UV flux, and therefore the OH
125 production rate, can be varied. We oxidized α -pinene with varying concentrations of O₃
126 and UV intensity, and in the presence and absence of effloresced ammonium sulfate seed
127 particles, as part of a more extensive measurement campaign (PANDA - Probing Aerosol
128 Nucleation During Alpha-pinene oxidation).

129

130 Here we present measurements at the end of the PANDA campaign when we utilized the
131 FIGAERO inlet system. Concurrent measurements were made of gas-phase ELVOC
132 (Ehn et al., 2014) using a nitrate-CIMS (Jokinen et al., 2012), 1 – 3 nm sized particles
133 with a Particle Size Magnifier (PSM, Airmodus, Finland), the number size distribution
134 from 3 – 600 nm using a Scanning Mobility Particle Sizer (SMPS TSI model 3071),
135 monoterpene concentrations using a quadrupole PTR-MS (Ionicon, Austria), and non-
136 refractory particle composition with a High-Resolution Aerosol Mass Spectrometer (HR-
137 AMS, Aerodyne, USA) (DeCarlo et al., 2006). We used the composition measured from
138 the AMS and total particle volume from a SMPS to calculate particle mass of sulfate and
139 SOA present in the chamber. The chamber was run in steady state mode with constant
140 addition of 30 ppb α -pinene and 80 ppb ozone. We began with α -pinene ozonolysis in the
141 dark followed by OH oxidation, where the OH was produced by shielded UV lamps
142 (Mentel et al., 2009). For both conditions, we added seed particles to increase the
143 particle/chamber wall surface ratio in order to better compete with condensation and
144 partitioning of low and semi-volatile gases to the chamber walls (Matsunaga and
145 Ziemann, 2010). We added effloresced (solid) ammonium sulfate particles with
146 concentrations spanning from 0 to 70 $\mu\text{g m}^{-3}$. Except for the period at $\sim 25 \mu\text{g m}^{-3}$
147 sulfate, most seed particle concentrations were a momentary state, i.e. steady-state was
148 not assessed, nor likely achieved for most components.

149

150 A University of Washington chamber was also used for optimization and initial testing of
151 the FIGAERO in steady-state conditions as well as batch mode experiments to explore
152 the time dependence of oxidation products. The chamber consists of a 0.7 m³ Teflon bag
153 with multiple sampling or fill ports. The chamber is pressure controlled by a servo-
154 controlled valve that regulates the draw of air out of the chamber held slightly above
155 atmospheric pressure ($\sim +1$ mb). The chamber is continuously filled with zero air,
156 generated by a Teledyne zero air generator (Model 701) and flow is set by a 20000 sccm
157 mass flow controller (MKS 1179a). α -Pinene is delivered by a perforated Teflon
158 diffusion tube held at room temperature, or a vial of pure α -Pinene in an ice bath, the
159 output from which mixes with the incoming zero air containing O₃ generated by passing

160 100 sccm of UHP N₂ with 10% O₂ through a UV photolysis cell. The α-pinene mass
161 loading in the chamber is set by the ratio of flows through the diffusion source and the
162 main chamber air. For the data discussed here, the RH of the UW chamber was < 5%.

163

164 **2.2 FIGAERO-HRToF-CIMS.** The FIGAERO and its HR-ToF-CIMS coupling has
165 been described in detail elsewhere (Lopez-Hilfiker et al., 2014), therefore only a review
166 of its general operation and differences from the standard operation are described here.
167 The FIGAERO is essentially a multi-port inlet assembly that allows sampling of either
168 gas phase components or thermally desorbed particulate compounds into a high-
169 resolution time of flight mass spectrometer (HR-ToF-CIMS) with selective detection by
170 chemical ionization. Here we present results using acetate negative-ion proton transfer
171 ionization (Veres et al., 2008). The instrument is continuously cycled between gas and
172 particle analysis modes with periodic determinations of the particle and gas-phase
173 background signals using a secondary filter (Lopez-Hilfiker et al., 2014).

174

175 A prototype of the FIGAERO-HRToF-CIMS was deployed at JPAC and installed
176 directly under the chamber in the temperature controlled chamber room. As the
177 FIGAERO was primarily designed for ambient sampling at high flows, for faster particle
178 concentration onto the filter, we reduced the flow rate across each of the inlets and
179 changed the inlet tube diameters to be more appropriate for the low flow conditions
180 required on the chamber, which has a finite fill rate. At JPAC, chamber air was drawn at
181 10 slpm from the base of the chamber through a 1.5 m long 10 mm OD stainless steel
182 tube. About 1 m of the tube extended into the center of the chamber, and the other 0.5 m
183 spanned from the chamber edge to a manifold located at the instrument. Approximately 2
184 slpm was drawn from this manifold to sample the gas-phase composition via a 6.5 mm
185 OD PTFE inlet with a length of approximately 12 cm to the HRToF-CIMS. Another 5
186 slpm was drawn from the manifold via a 20 cm length of 6.5 mm OD copper tube across
187 the primary FIGAERO filter to collect particles. We collected particles for 30 minutes at
188 5 slpm and thermally desorbed the particles for 40 minutes at a ramp rate of 20 °C/min
189 from ambient to 200 °C at which point the temperature was held constant to ensure that
190 particle phase signals returned to their pre-heating levels. The particle sample flow is

191 monitored by a mass flow meter (MKS 1179a) to track the total volume sampled over the
192 collection period and relates the integrated particle desorption signal area to a mass
193 loading in the chamber.

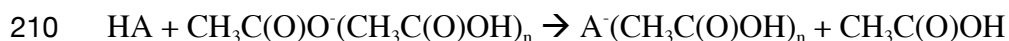
194

195 To assess the particle background due to adsorption and/or absorption of gases onto the
196 Teflon filter, we manually placed an identical filter in a Teflon filter holder immediately
197 upstream of the FIGAERO filter. Particle backgrounds were conducted at each
198 photochemical condition in the chamber, usually multiple times, to obtain representative
199 backgrounds at each stage. Gas-phase backgrounds were assessed at the point prior to
200 desorption when the instrument is sampling UHP N₂, and also when the pre-filter was in
201 place which allows for assessing whether particle components volatilized in the heated
202 portions of the IMR and transfer tubing between the prototype FIGAERO filter and the
203 IMR.

204

205 **2.3 Acetate Chemical Ionization.** The measurements reported here were obtained using
206 acetate ionization, employed as described previously (Mohr et al., 2013; Veres et al.,
207 2008; Yatavelli et al., 2012). The dominant ionization mechanism is expected to be
208 proton abstraction governed by the gas-phase pK_a of a compound relative to acetic acid.

209



211

212 The reagent ion cluster distribution is unknown for our conditions, but tests changing the
213 collisional declustering after the ionization region indicate n=1 with some minor
214 contribution from n=2 or higher. The collisional declustering strength is set such that
215 ~99% of the reagent ion is detected as n=0, and <1% as n=1 or higher. Thus, ion-neutral
216 clusters are likely to be minor components of the ion signal. The sensitivity of the
217 instrument was periodically calibrated during the JPAC campaign by adding the output of
218 a formic acid permeation device to the inlet. The permeation device output was calibrated
219 gravimetrically before and after the measurements.

220

221 The acetate chemical ionization scheme is still relatively novel, and as such, its
222 selectivity and sensitivity towards a large range of compounds and functional groups
223 remains to be characterized. For this reason, we performed a series of calibrations after
224 the measurement campaign to investigate the sensitivity of acetate ionization to a series
225 of carboxylic acids, RC(O)OH, and related functional groups, such as peroxy acids,
226 RC(O)O-OH, and a diacyl peroxide (benzoyl peroxide), see Figure 1. In all cases,
227 compounds were calibrated as described previously (Mohr et al., 2013). For these tests,
228 the walls of the ion-molecule reaction (IMR) region were heated to 60 °C – though it is
229 unlikely the gas equilibrates to that temperature for the ~ 100 ms of transit through the
230 region. While limited in number and type, the compounds tested to date suggest that
231 acetate ionization, as employed in our instrument, converts peroxy acids to the
232 corresponding carboxylate anion with nearly the same efficiency as the corresponding
233 carboxylic acids. In addition, benzoyl peroxide is detected at the benzoate anion more
234 efficiently than is benzoic acid. Other functional groups, e.g. polyols and esters, were not
235 detected nearly as efficiently, nor were clusters of the tested components with acetate
236 ions detected at significant signals. Thus, we conclude, perhaps conservatively, that
237 acetate ionization is a measure of functionalities that can easily produce carboxylate
238 anions, such as peroxy acids and di-acyl peroxides in addition to carboxylic acids under
239 the operating conditions used here.

240

241 For compounds with a carboxyl-related group, there appears to be a convergence of
242 sensitivity towards a maximum value similar to that for formic acid (see Figure 1). Given
243 the available evidence, using this maximum sensitivity value for the entire spectrum
244 would presumably lead to a lower-limit estimate of the mass concentrations of such
245 compounds in the chamber. Clearly, further investigation and optimization of acetate
246 ionization selectivity is needed, as is care attributing any signal to a specific functionality
247 measured with acetate ionization. That said, our main conclusions are not dependent upon
248 the exact functional groups acetate detects.

249

250 **3. Results**

251 **3.1 Contribution of Acyl containing compounds to α -Pinene SOA**

252 Figure 2 shows an overview of the key aerosol measurements during the time when the
253 FIGAERO was installed at JPAC. As the surface area concentration of the seed particles
254 increased, the detected AMS organic aerosol mass increased while the amount of
255 monoterpene reacted remained constant. Consequently, during ozonolysis conditions, the
256 inferred SOA mass yield increased from 1% to 10% even though the α -pinene reacted
257 remained constant. Similarly, the inferred SOA mass yield nearly doubled during OH
258 oxidation of constant $\Delta(\alpha$ -pinene) just by adding seed particles. The absolute abundance
259 of detected compounds in the particle-phase, measured by the FIGAERO, also increases
260 with the addition of seed, and is highly correlated with the total SOA measured by the
261 AMS at all times. However, the fractional contribution of “acyl-containing” compounds
262 to SOA changes little over the varying SOA mass concentration and oxidant conditions
263 (inset Figure 2).

264

265 To make the comparison between the FIGAERO-HRToF-CIMS and AMS quantitative,
266 we used the sensitivity of the instrument to formic acid (ions/sec per mole/m³) as a
267 measure of the average sensitivity to all detected compounds. Based on the data shown in
268 Figure 1, this assumption is reasonable to within a factor of 1.5 as governed by the spread
269 of calibration factors to individual compounds, especially in the m/Q range where much
270 of the particle phase mass is detected. We include in the analysis only ions having a
271 molecular formula (C_xH_yO_z) that contain at least one degree of unsaturation, an odd
272 number of H atoms and at least two O atoms. This selection represents the vast majority
273 of signal measured during these experiments (>85%). We convert the integrated
274 thermograms of each ion to $\mu\text{g m}^{-3}$ using the formic acid sensitivity, the molecular mass
275 of the ion plus the mass of one H, and the volume of air sampled prior to the thermogram
276 measurement (see *Lopez-Hilfiker, et al. (2014)* for more details). The resulting total
277 signal accounts for 25 – 50% of the organic aerosol measured by the AMS. We discuss
278 the volatility distribution and phase partitioning of this significant fraction of OA below.

279

280 **3.2 Gas-Particle Partitioning: Measurement, theory, and the role of thermal**
281 **decomposition.**

282 As the FIGAERO allows measurement of compounds in both gas and particle phase, we
283 are able to assess the phase partitioning directly of individual molecular compositions,
284 after accounting for the volumetric concentration in the particle phase inlet relative to the
285 instantaneous gas phase measurement. To calculate the phase partitioning, we follow a
286 similar procedure to that of *Yatavelli et al. 2014*, defining fraction in the particle phase
287 (F_p) as the concentration in the particle phase divided by the sum of gas and particle
288 phases (Equation 1) for a given ion elemental composition. Because the HR-ToF-CIMS
289 does not resolve structural isomers, this approach implicitly assumes that all isomers with
290 the same elemental composition have the same saturation vapor pressures and activity
291 coefficients. Before evaluating phase-partitioning, we first assess this assumption by
292 performing an analysis of the thermal desorption profiles, i.e. “thermograms”, for specific
293 ion compositions.

294 In Figure 3 (top panels), we show the thermal desorption profiles for two molecular
295 compositions, $C_8H_{12}O_4$ (left) and $C_9H_{14}O_4$ (right) consistently measured as major
296 components of the detected monoterpene SOA. For the purposes of comparing to a phase
297 partitioning model below, we assume these compositions represent common pinene
298 derived acids – pinic and norpinic acid, though terpenylic acid (Yasmeen et al., 2010) is
299 also a possibility for the latter. As shown in our previous work (Lopez-Hilfiker et al.,
300 2014), thermograms of compounds desorbing from synthetic mixtures deposited on the
301 filter exhibit fairly uniform, single-mode desorption profiles, with signal maxima
302 occurring at distinct desorption temperatures which correlate with a compound’s enthalpy
303 of sublimation. In contrast, the multi-modal form of the thermograms of individual α -
304 pinene SOA components suggest these thermograms contain added chemical information,
305 either about the presence of isomers with vastly different heats of vaporization (vapor
306 pressures) or higher molecular mass and lower volatility compounds that thermally
307 decompose into the compositions which are measured by the HR-ToF-CIMS.

308 To further investigate the sources of, and thus information carried by, the more complex
309 desorption features observed in the α -pinene SOA (shoulders, multiple modes, enhanced
310 tailing, etc), we applied a custom non-linear least squares peak-fitting routine to the
311 thermograms. First, single-mode thermogram peaks are identified and standardized on a

312 normalized width scale. The resulting normalized peaks are averaged to obtain a typical
313 thermogram peak shape that represents the desorption profile of a single component. An
314 iterative routine using the Levenberg-Marquardt algorithm for nonlinear least squares
315 problems fits the multimodal thermograms by applying a variable number of thermogram
316 peaks having the average desorption peak shape. The number, location and amplitude of
317 each additional desorption peak within a thermogram are optimized to explain the total
318 thermogram of a given ion. To allow for individual compounds having slightly different
319 desorption profiles, the width of the typical desorption peak shape is allowed to vary by
320 up to 30% based on fitting a range of thermograms from pure component desorptions.

321 Typical results from this thermogram fitting routine are shown in the top panels of Figure
322 3. Two or three separate particle phase components are desorbing as $C_8H_{12}O_4$ (“norpinic”) and
323 $C_9H_{14}O_4$ (“pinic”) at distinctly different temperatures. Blue areas represent the
324 fraction of the detected mass desorbing at lower temperatures and which would be
325 consistent with desorption temperatures expected for norpinic or pinic acid volatilities
326 based on our relationship between enthalpy of sublimation (vapor pressure) and
327 desorption temperature (Lopez-Hilfiker et al., 2014). In red, we show the contribution of
328 secondary modes to the overall thermogram that occur at much higher temperatures than
329 expected for these compounds. There is a third possible intermediate bin, but its presence
330 is always much smaller and not statistically significant across the full time series, and so
331 it is not included in the time series discussed below. Based on our calibrated desorption
332 temperature axis, the two major portions of the thermograms correspond to order-of-
333 magnitude effective 298 K saturation vapor pressures of $\sim 10^{-4}$, and $\sim 10^{-10}$ Pa (or C^* of
334 ~ 10 and $\sim 10^{-6}$ $\mu\text{g}/\text{m}^3$). As it is highly unlikely that there would be two structural isomers
335 (one for norpinic and one for pinic acid) both with 6 orders of magnitude lower vapor
336 pressures than the other isomers, we conclude that the secondary desorption events are
337 caused by larger molecular weight compounds, e.g. oligomeric accretion reaction
338 products, thermally decomposing to compounds with the same compositions as norpinic
339 and pinic acid that subsequently desorb and are detected by the HR-ToF-CIMS. Large
340 macromolecules are of sufficiently low volatility that the enthalpy of vaporization is very
341 likely larger than the dissociation energies of their weakest bonds, leading to preferential

342 decomposition into smaller components (e.g., oligomeric building blocks) instead of
343 evaporation. For example, we note here that a typical O-O bond energy (one of the
344 weaker organic covalent bonds) is ~ 140 kJ/mol (Blanksby and Ellison, 2003; Epstein et
345 al., 2010), which corresponds to a desorption temperature of ~ 80 °C based on our
346 calibration of sublimation enthalpy, though other thermal decomposition processes are of
347 course possible. This idea is consistent with previous work using a TPTD which also
348 investigated the multimodal nature of thermally desorbed SOA from the reaction of α -
349 pinene and ozone (Docherty et al., 2005) which concluded a large fraction of the SOA
350 formed consisted of organic peroxides.

351

352 In the bottom panels of Figure 3 we show the time series of the fractional contribution
353 each of the fitted desorption peaks makes to the overall thermogram area. Interestingly,
354 the lower volatility secondary modes in the thermal desorption of norpinic and pinic acids
355 are more prominent during ozonolysis than OH dominated oxidation of α -pinene. Despite
356 increased overall production (mass loading) of pinic and norpinic acids during OH
357 dominated oxidation, the secondary modes are much less important, especially in the
358 pinic acid case. Aside from providing a potential mechanistic insight into the chemical
359 origins of these lower volatility compounds, their varying importance due to a change
360 only in the chamber photochemical conditions suggests that these secondary modes are
361 likely not an artifact of the desorption process but rather are evidence for lower volatility
362 components that decompose into the C_8 and C_9 acids.

363

364 With the above insights into the thermal desorption process, we can more accurately
365 assess gas-particle partitioning. We use equilibrium partitioning theory first described by
366 *Pankow* (Pankow, 1994) to model the phase partitioning of three monoterpene derived
367 acids: pinic, norpinic, and pinonic acids. Equation 2 shows the transformation of
368 equilibrium partitioning theory to a formulation of fraction in the particle phase (F_p) that
369 we use to evaluate the quality of agreement between modeled and measured partitioning.

370

$$371 \quad F_p = \frac{\text{Particle}}{\text{Gas+Particle}} \quad (\text{Eq. 1})$$

372

373
$$F_p = \left(1 + \frac{M_{10}^6 \zeta P}{760 RT C_{OA}} \right)^{-1} \quad (\text{Eq. 2})$$

374

375 In Equation 2, C_{OA} ($\mu\text{g m}^{-3}$) is the organic aerosol mass concentration, M (g mol^{-1}) is the
376 molar mass of the compound of interest, ζ is the activity coefficient, which we assume is
377 unity (and discuss later in detail), P (torr) is the vapor pressure of compound the over the
378 pure component, R ($8.2 \times 10^{-5} \text{ m}^3 \text{ atm K}^{-1} \text{ mol}^{-1}$) is the gas constant, T (K) is the
379 environmental temperature and 760 (torr atm^{-1}) and 10^6 ($\mu\text{g g}^{-1}$) are unit conversion
380 factors. As the JPAC chamber is held at fixed temperature (15 °C), the free variables in
381 Equation 2 become the total organic mass concentration, which was measured by the
382 AMS and SMPS, and the pure compound saturation vapor pressure. Using literature
383 values to constrain saturation vapor pressures, specifically those predicted by the
384 structure activity relationship of Capouet et al, we then evaluate whether or not
385 equilibrium adsorptive partitioning explains the observed phase partitioning for our
386 chamber conditions (Capouet and Müller, 2006).

387

388 Based on the thermogram analysis presented above, it is highly unlikely that norpinic and
389 pinic acid partitioning would be well described by an equilibrium partitioning model that
390 assumed all of the measured particle mass (thermogram area) carried in those two acids
391 was in equilibrium with the corresponding gas-phase acids. We demonstrate this issue in
392 Figure 4. In the top panels of Figure 4, we show the thermal desorption profiles for the
393 three molecular compositions, $\text{C}_9\text{H}_{14}\text{O}_4$, $\text{C}_{10}\text{H}_{16}\text{O}_3$, and $\text{C}_8\text{H}_{12}\text{O}_4$, from particles collected
394 under each set of conditions ($\text{O}_3 + \text{seed}$ and OH). Ozonolysis conditions are shown in
395 black, while OH oxidation conditions are shown in red. As above, we assume these
396 compositions correspond to pinic, pinonic acid, and norpinic acids, respectively. Pinonic
397 acid provides a useful contrast to the other two in that it does not show evidence for
398 secondary desorption peaks under either set of conditions.

399

400 Previous comparisons to adsorptive partitioning models have used the full integrated
401 thermogram arising from thermal desorption to compare with the model prediction and
402 found varying levels of agreement (Yatavelli et al., 2014; Zhao et al., 2013). In the

403 middle panels of Figure 4, we plot the measured F_p , calculated from the full integral of
404 the thermogram, *versus* the F_p predicted by the adsorptive partitioning model. The points
405 are colored by experiment time, with reddish points corresponding to OH oxidation
406 towards the end of the experiment and all other colors (blueish) corresponding to
407 ozonolysis conditions. Generally poor agreement is observed, highlighted by non-
408 linearity, and by points falling far from the 1:1 line. There is one exception: pinic acid
409 during OH oxidation (red points). This condition is also when the thermogram for the
410 composition corresponding to pinic acid is largely a single mode (see Figure 4 top),
411 suggesting that if the thermograms are deconvolved into contributions representing the
412 different modes, the agreement between measured and predicted F_p would improve.

413

414 In the lower panels of Figure 4 we show the results of deconvolving the thermograms
415 into the different modes using the above fitting approach for a more direct test of the
416 actual partitioning of these three acids into the particle phase. Based on our previous
417 work, compounds with compositions similar to those under consideration here, C_8 - C_{10}
418 keto and diacids, would have thermogram signals that maximize at a desorption
419 temperature (T_{max}) of 80 °C, or below, if they were non-interacting components of a
420 solution (Lopez-Hilfiker et al., 2014). Therefore, in our revised partitioning analysis, we
421 assume that in order to be in dynamic equilibrium with the gas-phase, a compound should
422 desorb from the particle-phase at a temperature consistent with its expected enthalpy of
423 sublimation. Thus, we use only a portion of the area under the thermogram to calculate
424 the particle-phase concentration of each acid in equilibrium with that in the gas-phase. In
425 this case, that area corresponds to the desorption mode at the lowest temperature in the
426 thermogram analysis. The other peaks and shoulders in the thermograms that arise at
427 significantly higher temperatures are presumably from processes related to thermal
428 decomposition and/or high temperature formation of acid functionalities which produce
429 the molecular “fragments” detected by the CIMS. The abundance of these molecular
430 “fragments” from lower volatility components would have no direct impact on the
431 equilibrium partitioning of the actual $C_8 - C_{10}$ acids. Accounting for these structures in
432 the thermograms leads to much better agreement (pinic acid: $R^2 = 0.8$, slope = 0.99,
433 intercept -0.07, norpinic acid: $R^2 = 0.92$, slope = 0.78, intercept -0.04) between the

434 partitioning model and measured F_p for pinic and norpinic acids across all chamber
435 conditions, suggesting that *i*) literature estimates of their saturation vapor pressures used
436 herein are reasonable, that *ii*) Raoult's Law based partitioning is applicable under the
437 chamber conditions, and therefore that *iii*) particle viscosities can't be so high as to
438 disrupt the equilibration process on the \sim hour timescale of the chamber measurements.

439

440 The revised partitioning calculation, using the thermogram fitting approach, does not
441 improve the measurement-model agreement for pinonic acid. Pinonic acid desorbs as a
442 single peak under all conditions, therefore providing no basis for selecting a smaller
443 portion of the thermogram area. Yet, pinonic acid clearly desorbs from the α -pinene SOA
444 at a temperature ($T_{\max} \sim 40$ °C) that is significantly higher than if placed on the filter in
445 pure form (or part of a synthetic mixture), where it desorbs at $T_{\max} \ll 32$ °C (Lopez-
446 Hilfiker et al., 2014). Our measurements therefore suggest that the effective vapor
447 pressure of pinonic acid is lowered over the SOA ($F_p^{\text{measured}} \gg F_p^{\text{predicted}}$) relative to over
448 the pure substance or an ideal solution. As the temperature of maximum desorption for
449 pinonic acid from the α -pinene SOA is less than that required to break the weakest of
450 covalent bonds, and because the thermogram is a single mode, it is unlikely that the
451 pinonic acid desorption arises from the same processes that we hypothesize give rise to
452 the secondary peaks in the thermograms of pinic and norpinic acids. We note that there
453 are potentially lower energy pathways to decomposition than a typical bond strength
454 analysis might suggest, and therefore decomposition can't easily be ruled out. However,
455 the measurement-model agreement is highly linear, suggesting a single adjustment in the
456 pinonic acid vapor pressure, i.e. an activity coefficient different from unity ($\sim .25$), would
457 bring agreement under most conditions (see Figure 4 bottom). Enhanced H-bonding of
458 pinonic acid in the multi-functional SOA environment relative to the pure substance
459 could explain these behaviors.

460

461 We conclude this section by noting that thermal decomposition of particulate organic
462 material likely occurs in any technique that utilizes heat to drive compounds into the gas
463 phase for analysis. But, by utilizing a calibrated relationship between molecular
464 composition and desorption temperature, together with a slow desorption temperature

465 ramp rate, the effects of thermal decomposition on inferred vapor pressure driven
466 partitioning can be addressed and even utilized to arrive at a more complete view of SOA
467 composition and volatility as we demonstrate below.

468

469 **3.3 Bulk Aerosol Volatility**

470 Above we provided specific examples of how a consistent framework can be used to
471 relate SOA molecular composition and vapor pressure driven partitioning to thermal
472 desorption measurements. However, as shown in Figure 5a, we observe many (hundreds)
473 of compounds which desorb at much higher temperatures from α -pinene ozonolysis SOA
474 than consistent with their composition. These particular data were obtained from
475 analyzing α -pinene ozonolysis SOA generated in the UW chamber under steady-state
476 continuous-flow conditions. The points are sized by the *square-root* (for dynamic range)
477 of the particle mass concentration for each molecular composition detected and colored
478 by its thermogram T_{\max} . A swath of compounds containing 1 to 5 carbon atoms all desorb
479 at temperatures between 50 - 90 °C, similar to much lower volatility compounds such as
480 C_8 - C_{10} diacids, and certainly inconsistent with expected heats of vaporization for those
481 small compounds. We hypothesize that this whole group of compounds (light blue)
482 results from decomposition of larger molecules or from weakly bound complexes that
483 effectively lower the vapor pressures of these smaller compounds.

484

485 The simplest way to organize and reduce the information in Figure 5a is by summing the
486 calibration adjusted signal across all detected compounds. We show an example of the
487 resulting sum thermogram in Figure 5b. Using the thermogram fitting approach discussed
488 above, and our previously determined volatility axis based on desorption temperature, we
489 can examine the bulk volatility of the α -pinene ozonolysis SOA detected by the
490 FIGAERO HR-ToF-CIMS from the sum thermogram. We find that three volatility modes
491 are required to explain the sum thermogram. The first mode is centered at ~ 60 °C,
492 consistent with volatilities of C_8 - C_{10} diacids ($C^* \sim 1 - 10 \text{ ug/m}^3$). This mode represents \sim
493 50% of the measured desorption signal. Two other modes are apparent at higher
494 desorption temperatures, one maximizing at ~ 110 °C and the other at ~ 150 °C. Clearly, a
495 large fraction of the total mass of detected compounds desorbing from the α -pinene SOA

496 are from very low volatility components. In the upper panel of Figure 5, these higher
497 temperature modes correspond to the appearance of $C_{15} - C_{20}$ compounds, lending
498 support to the conclusion that large molecular weight accretion products are a source of
499 the smaller molecular components that also maximize at higher temperatures. Roughly
500 50% of the signal measured during a desorption occurs at temperatures greater than
501 100 °C, corresponding to effective $C^* < 10^{-5} \text{ ug m}^{-3}$.

502

503 The above estimates of C^* values and carbon mass associated with them are probably
504 upper and lower limits, respectively, because extremely low volatility compounds likely
505 decompose before desorbing, which biases the measured volatility higher, and the acetate
506 ionization scheme may not be sensitive to all of the decomposition fragments, which
507 biases the detected mass lower.

508

509 **4. Discussion**

510 From an analysis of molecular thermograms of α -pinene SOA generated in chambers, we
511 find that a large fraction of the characterized SOA is of very low volatility, with
512 compositions having $>10 \text{ C}$, and $> 4 \text{ O}$. Moreover, we find that acetate ionization can
513 explain at least 25 – 50% of the total SOA. We conclude that large molecular weight
514 compounds must be present in the aerosol. Indeed, we directly observe compounds with
515 up to as many as 30 carbon atoms and up to 10 oxygen atoms desorbing from the α -
516 pinene SOA. Additional indirect evidence is that commonly reported oxidation products
517 of α -pinene, such as pinic, norpinic, and other carboxylic acids desorb at temperatures far
518 too high to be consistent with their expected enthalpies of vaporization. Treating all of
519 the mass that desorbs from the particles in the form of these common and smaller
520 products as being in vapor pressure driven equilibrium with the corresponding gas-phase
521 compounds leads to large errors between modeled and measured gas-particle partitioning
522 that cannot be explained by a simple adjustment of the saturation vapor concentration nor
523 its temperature dependence. Moreover, that some 50% or more of the CIMS-detected
524 SOA mass is effectively non-volatile, having $C^* < 10^{-5} \text{ ug/m}^3$, conflicts with previous
525 conclusions that α -pinene ozonolysis SOA is predominantly semi-volatile (An et al.,

526 2007; Hallquist et al., 2009) but could be consistent with recent evidence that α -pinene
527 SOA might be semisolid (Renbaum-Wolff et al., 2013).

528

529 Our findings are broadly similar with other online and offline molecular characterizations
530 of α -pinene SOA, which have found evidence for oligomeric compounds (DePalma et al.,
531 2013; Gao et al., 2004; Hall and Johnston, 2011; 2012). Our approach combines slow
532 temperature ramps and molecular characterization without chromatography and thus
533 provides a compliment to methods that have observed oligomeric material using liquid
534 extraction followed by chromatography and electrospray ionization, or particle beam
535 thermal desorption coupled to electron impact ionization (Ziemann, 2002). We provide
536 an additional constraint on the fraction of SOA that is contained in these oligomeric
537 compounds and how that fraction varies in response to different photochemical regimes.

538

539 The addition of OH and UV light suppresses the secondary low volatility modes in the
540 thermograms of pinic and norpinic acids, which suggests that the products formed via
541 accretion chemistry may be susceptible to photolysis and reaction with OH, or involve a
542 precursor formed only during ozonolysis. The presence of peroxides as macromolecule
543 linkages is certainly consistent with our results, given that the secondary modes in
544 thermograms of many compounds arise at temperatures above the O-O bond strength, the
545 weakest covalent bond. That there might be a significant source of low volatility peroxide
546 compounds in α -pinene SOA was shown recently by Ehn et al. 2014. Whether the
547 oligomeric compounds we observe are from $\text{RO}_2 + \text{RO}_2$ reactions in the gas-phase or
548 from particle-phase accretion reactions such as peroxy hemiacetal formation, or some
549 combination thereof, is beyond the scope of this paper, but should be addressed in future
550 studies in order to more accurately represent their contribution to SOA in models
551 (Docherty et al., 2005; Ziemann and Atkinson, 2012).

552

553 We use an estimate of the O-O bond strength to put desorption temperature into a
554 chemical bond context, but the O-O bond strength will depend upon molecular structure,
555 and thus there is likely a distribution across the desorption temperature space of
556 molecular fragments desorbing at higher temperatures than their composition would

557 suggest due to O-O bond cleavage. Additionally, there may be other bond scission
558 pathways beyond the O-O functionality which we have not yet identified. The pinonic
559 acid thermogram is a possible example, desorbing from the α -pinene SOA at
560 temperatures well below the O-O bond strength equivalent but well above that expected
561 from its known enthalpy of vaporization. Non-covalent H-bonding within the SOA
562 matrix that is stronger or more ubiquitous than in pure single component samples or
563 simple ideal mixtures is another mechanism to explain lower than expected volatility.
564 Three persistent H-bonds would be equivalent to about half the bond strength of an O-O
565 bond (Dougherty, 1998). Oligomeric material may also be in thermodynamic equilibrium
566 with semi volatile material such that losses of semi-volatile compounds even at lower
567 temperatures than the weakest covalent or hydrogen bond could lead to decomposition of
568 oligomeric material to re-achieve equilibrium. Processes like these need not occur at high
569 temperatures but also may occur at near ambient temperatures. The FIGAERO approach
570 would potentially be able to capture this process if the evaporation rate of monomers was
571 large enough to produce detectable signal prior to ramping the temperature of the
572 desorption N_2 . That said, a majority of detected SOA mass desorbed at temperatures well
573 above covalent bond strengths.

574

575 Previous studies to characterize the molecular composition and partitioning of
576 atmospheric aerosol have observed small-oxygenated organics that were present in larger
577 than expected concentrations based on ideal partitioning. We show thermal
578 decomposition of large molecules can be a significant bias in thermal desorption
579 techniques resulting in smaller stable fragments that are then detected. The process of
580 thermal decomposition is likely common to any instrument which uses heat to drive
581 aerosol components into the gas phase for analysis (Holzinger et al., 2010; Smith et al.,
582 2010; Williams et al., 2006; Yatavelli et al., 2012; Zhao et al., 2013). Our measurements
583 utilizing the FIGAERO indicate that “small acids” present in higher than expected
584 concentrations in SOA are likely entirely due to thermal decomposition of much lower
585 volatility components of the aerosol.

586

587 **5. Conclusions**

588 We have explored the contribution, composition and volatility of acyl containing organic
589 compounds present in α -pinene derived secondary organic aerosol under atmospherically
590 relevant conditions using the FIGAERO HR-ToF-CIMS. The distribution of detected
591 compounds spanned C_{1-30} and O_{2-10} with many of the compounds that were detected in the
592 gas phase also present in the particle phase. The distribution of acyl containing
593 compounds in the particle phase explains at least 25% of the total SOA mass produced
594 under both OH oxidation and ozonolysis conditions and shows evidence for a significant
595 contribution from oligomers and other large macromolecules, especially during
596 ozonolysis. The volatility of the detected mass reflects this contribution, with a large
597 fraction of the organic mass having vapor pressures 4 orders of magnitude lower than
598 commonly detected diacid products from ozonolysis of α -pinene. In the particle analysis
599 we highlight the role of thermal decomposition, and show that, when it is accounted for
600 using the thermogram desorption profiles, equilibrium absorptive partitioning explains
601 well the observed phase partitioning of pinic and norpinic acids though a non-ideal
602 activity coefficient is required for pinonic acid under all conditions.

603

604 That we infer a significant fraction of the SOA is comprised of oligomeric compounds
605 given the relatively short residence times of the JPAC and UW chambers (45 – 60 min)
606 and the relatively small amount of α -pinene reacted in each case (~ 10 ppb), suggests
607 these types of compounds can play an important role in ambient monoterpene derived
608 SOA. If that is the case, it would imply that a significant fraction ($\sim 25\%$ or perhaps more)
609 of monoterpene ozonolysis SOA should be treated as effectively non-volatile in
610 atmospheric models. Future work utilizing the FIGAERO in the field will allow analysis
611 of ambient aerosol for comparison thereby providing a consistent view of SOA volatility
612 and composition that will provide a direct test of these conclusions.

613

614 **Acknowledgements**

615 We would like to thank the supporting staff and scientists at the Jülich Research Facility.
616 This work was supported by the US Department of Energy through awards from the
617 Atmospheric System Research (DOE Grant DE-SC0006867) and SBIR (DE-SC0004577)
618 programs.

619

620

621 References:

622

623 An, W. J., Pathak, R. K., Lee, B.-H. and Pandis, S. N.: Aerosol volatility measurement
624 using an improved thermodenuder: Application to secondary organic aerosol, *Journal of*
625 *Aerosol Science*, 38(3), 305–314, doi:10.1016/j.jaerosci.2006.12.002, 2007.

626 Blanksby, S. J. and Ellison, G. B.: Bond Dissociation Energies of Organic Molecules,
627 *Acc. Chem. Res.*, 36(4), 255–263, doi:10.1021/ar020230d, 2003.

628 Capouet, M. and Müller, J. F.: A group contribution method for estimating the vapour
629 pressures of α -pinene oxidation products, *Atmos. Chem. Phys.*, 6(6), 1455–1467,
630 doi:10.5194/acp-6-1455-2006, 2006.

631 Cappa, C. D.: A model of aerosol evaporation kinetics in a thermodenuder, *Atmos. Meas.*
632 *Tech.*, 3(3), 579–592, doi:10.5194/amt-3-579-2010-supplement, 2010.

633 Cappa, C. D. and Jimenez, J. L.: Quantitative estimates of the volatility of ambient
634 organic aerosol, *Atmos. Chem. Phys.*, 10(12), 5409–5424, doi:10.5194/acp-10-5409-
635 2010, 2010.

636 DeCarlo, P. F., Kimmel, J. R., Trimborn, A., Northway, M. J., Jayne, J. T., Aiken, A. C.,
637 Gonin, M., Fuhrer, K., Horvath, T., Docherty, K. S., Worsnop, D. R. and Jimenez, J. L.:
638 Field-Deployable, High-Resolution, Time-of-Flight Aerosol Mass Spectrometer, *Anal.*
639 *Chem.*, 78(24), 8281–8289, doi:10.1021/ac061249n, 2006.

640 DePalma, J. W., Horan, A. J., Hall, W. A., IV and Johnston, M. V.: Thermodynamics of
641 oligomer formation: implications for secondary organic aerosol formation and reactivity,
642 *Phys. Chem. Chem. Phys.*, 15(18), 6935, doi:10.1039/c3cp44586k, 2013.

643 Docherty, K. S., Wu, W., Lim, Y. B. and Ziemann, P. J.: Contributions of Organic
644 Peroxides to Secondary Aerosol Formed from Reactions of Monoterpenes with O₃,
645 *Environ. Sci. Technol.*, 39(11), 4049–4059, doi:10.1021/es050228s, 2005.

646 Donahue, N. M., Epstein, S. A., Pandis, S. N. and Robinson, A. L.: A two-dimensional
647 volatility basis set: 1. organic-aerosol mixing thermodynamics, *Atmos. Chem. Phys.*,
648 11(7), 3303–3318, doi:10.5194/acp-11-3303-2011, 2011.

649 Dougherty, R. C.: Temperature and pressure dependence of hydrogen bond strength: A
650 perturbation molecular orbital approach, *J. Chem. Phys.*, 109(17), 7372,
651 doi:10.1063/1.477343, 1998.

652 Ehn, M., Thornton, J. A., Kleist, E., Sipilä, M., Junninen, H., Pullinen, I., Springer, M.,
653 Rubach, F., Tillmann, R., Lee, B., Lopez-Hilfiker, F., Andres, S., Acir, I.-H., Rissanen,
654 M., Jokinen, T., Schobesberger, S., Kangasluoma, J., Kontkanen, J., Nieminen, T.,
655 Kurtén, T., Nielsen, L. B., Jørgensen, S., Kjaergaard, H. G., Canagaratna, M., Maso, M.
656 D., Berndt, T., Petäjä, T., Wahner, A., Kerminen, V.-M., Kulmala, M., Worsnop, D. R.,
657 Wildt, J. and Mentel, T. F.: A large source of low-volatility secondary organic aerosol,

658 Nature, 506(7489), 476–479, doi:10.1038/nature13032, 2014.

659 Epstein, S. A., Riipinen, I. and Donahue, N. M.: A Semiempirical Correlation between
660 Enthalpy of Vaporization and Saturation Concentration for Organic Aerosol, Environ. Sci.
661 Technol., 44(2), 743–748, doi:10.1021/es902497z, 2010.

662 Gao, S., Keywood, M., Ng, N. L., Surratt, J., Varutbangkul, V., Bahreini, R., Flagan, R.
663 C. and Seinfeld, J. H.: Low-Molecular-Weight and Oligomeric Components in Secondary
664 Organic Aerosol from the Ozonolysis of Cycloalkenes and α -Pinene, The Journal of
665 Physical Chemistry A, 108(46), 10147–10164, doi:10.1021/jp047466e, 2004.

666 Hall, W. A., IV and Johnston, M. V.: Oligomer Content of α -Pinene Secondary Organic
667 Aerosol, Aerosol Science and Technology, 45(1), 37–45,
668 doi:10.1080/02786826.2010.517580, 2011.

669 Hall, W. A., IV and Johnston, M. V.: The Thermal-Stability of Oligomers in Alpha-
670 Pinene Secondary Organic Aerosol, Aerosol Science and Technology, 46(9), 983–989,
671 doi:10.1080/02786826.2012.685114, 2012.

672 Hallquist, M., Wenger, J. C., Baltensperger, U., Rudich, Y., Simpson, D., Claeys, M.,
673 Dommen, J., Donahue, N. M., George, C., Goldstein, A. H., Hamilton, J. F., Herrmann,
674 H., Hoffmann, T., Iinuma, Y., Jang, M., Jenkin, M. E., Jimenez, J. L., Kiendler-Scharr,
675 A., Maenhaut, W., McFiggans, G., Mentel, T. F., Monod, A., Prevot, A. S. H., Seinfeld, J.
676 H., Surratt, J. D., Szmigielski, R. and Wildt, J.: The formation, properties and impact of
677 secondary organic aerosol: current and emerging issues, Atmos. Chem. Phys., 9(14),
678 5155–5236, doi:10.5194/acp-9-5155-2009, 2009.

679 Heald, C. L., Kroll, J. H., Jimenez, J. L., Docherty, K. S., DeCarlo, P. F., Aiken, A. C.,
680 Chen, Q., Martin, S. T., Farmer, D. K. and Artaxo, P.: A simplified description of the
681 evolution of organic aerosol composition in the atmosphere, Geophys. Res. Lett., 37(8),
682 L08803, doi:10.1029/2010GL042737, 2010.

683 Holzinger, R., Kasper-Giebl, A., Staudinger, M., Schauer, G. and Röckmann, T.:
684 Analysis of the chemical composition of organic aerosol at the Mt. Sonnblick observatory
685 using a novel high mass resolution thermal-desorption proton-transfer-reaction mass-
686 spectrometer (hr-TD-PTR-MS), Atmos. Chem. Phys., 10(20), 10111–10128,
687 doi:10.5194/acp-10-10111-2010, 2010.

688 Jokinen, T., Sipilä, M., Junninen, H., Ehn, M., Lönn, G., Hakala, J., Petäjä, T., Mauldin,
689 R. L., III, Kulmala, M. and Worsnop, D. R.: Atmospheric sulphuric acid and neutral
690 cluster measurements using CI-API-TOF, Atmos. Chem. Phys., 12(9), 4117–4125,
691 doi:10.5194/acp-12-4117-2012, 2012.

692 Lopez-Hilfiker, F. D., Mohr, C., Ehn, M., Rubach, F., Kleist, E., Wildt, J., Mentel, T. F.,
693 Lutz, A., Hallquist, M., Worsnop, D. and Thornton, J. A.: A novel method for online
694 analysis of gas and particle composition: description and evaluation of a Filter Inlet for
695 Gases and AEROSols (FIGAERO), Atmos. Meas. Tech., 7(4), 983–1001,

696 doi:10.5194/amt-7-983-2014, 2014.

697 Matsunaga, A. and Ziemann, P. J.: Gas-Wall Partitioning of Organic Compounds in a
698 Teflon Film Chamber and Potential Effects on Reaction Product and Aerosol Yield
699 Measurements, *Aerosol Science and Technology*, 44(10), 881–892,
700 doi:10.1080/02786826.2010.501044, 2010.

701 Mentel, T. F., Wildt, J., Kiendler-Scharr, A., Kleist, E., Tillmann, R., Dal Maso, M.,
702 Fisseha, R., Hohaus, T., Spahn, H., Uerlings, R., Wegener, R., Griffiths, P. T., Dinar, E.,
703 Rudich, Y. and Wahner, A.: Photochemical production of aerosols from real plant
704 emissions, *Atmos. Chem. Phys.*, 9(13), 4387–4406, doi:10.5194/acp-9-4387-2009, 2009.

705 Mohr, C., Lopez-Hilfiker, F. D., Zotter, P., Prévôt, A. S. H., Xu, L., Ng, N. L., Herndon,
706 S. C., Williams, L. R., Franklin, J. P., Zahniser, M. S., Worsnop, D. R., Knighton, W. B.,
707 Aiken, A. C., Gorkowski, K. J., Dubey, M. K., Allan, J. D. and Thornton, J. A.:
708 Contribution of Nitrated Phenols to Wood Burning Brown Carbon Light Absorption in
709 Detling, United Kingdom during Winter Time, *Environ. Sci. Technol.*,
710 130610071812007, doi:10.1021/es400683v, 2013.

711 Pankow, J. F.: An absorption model of gas/particle partitioning of organic compounds in
712 the atmosphere, *Atmospheric Environment*, 28(2), 185–188, doi:10.1016/1352-
713 2310(94)90093-0, 1994.

714 Renbaum-Wolff, L., Grayson, J. W., Bateman, A. P., Kuwata, M., Sellier, M., Murray, B.
715 J., Shilling, J. E., Martin, S. T. and Bertram, A. K.: Viscosity of α -pinene secondary
716 organic material and implications for particle growth and reactivity, *Proceedings of the*
717 *...*, 2013.

718 Riccobono, F., Schobesberger, S., Scott, C. E., Dommen, J., Ortega, I. K., Rondo, L.,
719 Almeida, J., Amorim, A., Bianchi, F., Breitenlechner, M., David, A., Downard, A.,
720 Dunne, E. M., Duplissy, J., Ehrhart, S., Flagan, R. C., Franchin, A., Hansel, A., Junninen,
721 H., Kajos, M., Keskinen, H., Kupc, A., Kürten, A., Kvashin, A. N., Laaksonen, A.,
722 Lehtipalo, K., Makhmutov, V., Mathot, S., Nieminen, T., Onnela, A., Petäjä, T., Praplan,
723 A. P., Santos, F. D., Schallhart, S., Seinfeld, J. H., Sipilä, M., Spracklen, D. V., Stozhkov,
724 Y., Stratmann, F., Tomé, A., Tsagkogeorgas, G., Vaattovaara, P., Viisanen, Y., Vrtala, A.,
725 Wagner, P. E., Weingartner, E., Wex, H., Wimmer, D., Carslaw, K. S., Curtius, J.,
726 Donahue, N. M., Kirkby, J., Kulmala, M., Worsnop, D. R. and Baltensperger, U.:
727 Oxidation products of biogenic emissions contribute to nucleation of atmospheric
728 particles, *Science*, 344(6185), 717–721, doi:10.1126/science.1243527, 2014.

729 Riipinen, I., Yli-Juuti, T., Pierce, J. R., Petäjä, T., Worsnop, D. R., Kulmala, M. and
730 Donahue, N. M.: The contribution of organics to atmospheric nanoparticle growth,
731 *Nature Geosci*, 5(7), 453–458, doi:10.1038/ngeo1499, 2012.

732 Roldin, P., Eriksson, A. C., Nordin, E. Z., Hermansson, E., Mogensen, D., Rusanen, A.,
733 Boy, M., Swietlicki, E., Svenningsson, B., Zelenyuk, A. and Pagels, J.: Modelling non-
734 equilibrium secondary organic aerosol formation and evaporation with the aerosol

735 dynamics, gas- and particle-phase chemistry kinetic multilayer model ADCHAM, *Atmos.*
736 *Chem. Phys.*, 14(15), 7953–7993, doi:10.5194/acp-14-7953-2014-supplement, 2014.

737 Russell, L. M., Bahadur, R. and Ziemann, P. J.: Identifying organic aerosol sources by
738 comparing functional group composition in chamber and atmospheric particles,
739 *Proceedings of the National Academy of Sciences*, 108(9), 3516–3521,
740 doi:10.1073/pnas.1006461108, 2011.

741 Smith, J. N., Barsanti, K. C., Friedli, H. R., Ehn, M., Kulmala, M., Collins, D. R.,
742 Scheckman, J. H., Williams, B. J. and McMurry, P. H.: Observations of aminium salts in
743 atmospheric nanoparticles and possible climatic implications, *Proceedings of the National*
744 *Academy of Sciences*, 107(15), 6634–6639, doi:10.1073/pnas.0912127107, 2010.

745 Veres, P., Roberts, J. M., Burling, I. R., Warneke, C., de Gouw, J. and Yokelson, R. J.:
746 Measurements of gas-phase inorganic and organic acids from biomass fires by negative-
747 ion proton-transfer chemical-ionization mass spectrometry, *J. Geophys. Res.*, 115(D23),
748 doi:10.1029/2010JD014033, 2010.

749 Veres, P., Roberts, J. M., Warneke, C., Welsh-Bon, D., Zahniser, M., Herndon, S., Fall, R.
750 and de Gouw, J.: Development of negative-ion proton-transfer chemical-ionization mass
751 spectrometry (NI-PT-CIMS) for the measurement of gas-phase organic acids in the
752 atmosphere, *International Journal of Mass Spectrometry*, 274(1-3), 48–55,
753 doi:10.1016/j.ijms.2008.04.032, 2008.

754 Volkamer, R., Jimenez, J. L., San Martini, F., Dzepina, K., Zhang, Q., Salcedo, D.,
755 Molina, L. T., Worsnop, D. R. and Molina, M. J.: Secondary organic aerosol formation
756 from anthropogenic air pollution: Rapid and higher than expected, *Geophys. Res. Lett.*,
757 33(17), L17811, doi:10.1029/2006GL026899, 2006.

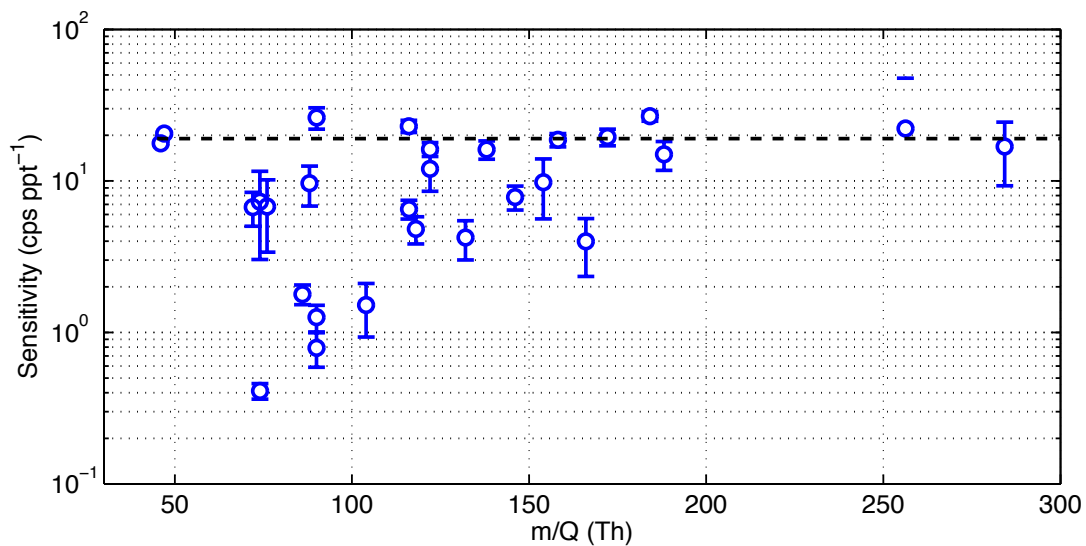
758 Williams, B. J., Goldstein, A. H., Kreisberg, N. M. and Hering, S. V.: An In-Situ
759 Instrument for Speciated Organic Composition of Atmospheric Aerosols: Thermal
760 Desorption Aerosol GC/MS-FID (TAG), *Aerosol Science and Technology*, 40(8), 627–
761 638, doi:10.1080/02786820600754631, 2006.

762 Yasmeen, F., Vermeylen, R., Szmigielski, R., Iinuma, Y., Böge, O., Herrmann, H.,
763 Maenhaut, W. and Claeys, M.: Terpenylic acid and related compounds: precursors for
764 dimers in secondary organic aerosol from the ozonolysis of α - and β -pinene,
765 *Atmos. Chem. Phys.*, 10(19), 9383–9392, doi:10.5194/acp-10-9383-2010-supplement,
766 2010.

767 Yatavelli, R. L. N., Lopez-Hilfiker, F., Wargo, J. D., Kimmel, J. R., Cubison, M. J.,
768 Bertram, T. H., Jimenez, J. L., Gonin, M., Worsnop, D. R. and Thornton, J. A.: A
769 Chemical Ionization High-Resolution Time-of-Flight Mass Spectrometer Coupled to a
770 Micro Orifice Volatilization Impactor (MOVI-HRToF-CIMS) for Analysis of Gas and
771 Particle-Phase Organic Species, *Aerosol Science and Technology*, 46(12), 1313–1327,
772 doi:10.1080/02786826.2012.712236, 2012.

- 773 YataVELLI, R., Stark, H. and Thompson, S. L.: Semicontinuous measurements of gas-
774 particle partitioning of organic acids in a ponderosa pine forest using a MOVI-HRToF-
775 CIMS, Atmospheric ..., 2014.
- 776 Zhao, Y., Kreisberg, N. M., Worton, D. R., Isaacman, G., Weber, R. J., Liu, S., Day, D.
777 A., Russell, L. M., Markovic, M. Z., VandenBoer, T. C., Murphy, J. G., Hering, S. V. and
778 Goldstein, A. H.: Insights into Secondary Organic Aerosol Formation Mechanisms from
779 Measured Gas/Particle Partitioning of Specific Organic Tracer Compounds, Environ. Sci.
780 Technol., 47(8), 3781–3787, doi:10.1021/es304587x, 2013.
- 781 Ziemann, P. J.: Evidence for Low-Volatility Diacyl Peroxides as a Nucleating Agent and
782 Major Component of Aerosol Formed from Reactions of O₃ with Cyclohexene and
783 Homologous Compounds, The Journal of Physical Chemistry A, 106(17), 4390–4402,
784 doi:10.1021/jp012925m, 2002.
- 785 Ziemann, P. J. and Atkinson, R.: Kinetics, products, and mechanisms of secondary
786 organic aerosol formation, Chem. Soc. Rev., 41(19), 6582, doi:10.1039/c2cs35122f, 2012.
- 787
- 788

789



790

791 Figure 1. The distribution of observed sensitivities to carboxylic acids using acetate
792 reagent ions. Error bars are 1 σ based on multiple injections of solutions following *Mohr*
793 *et al. 2013*. The black dashed line shows the sensitivity value used for bulk analysis.

794

795

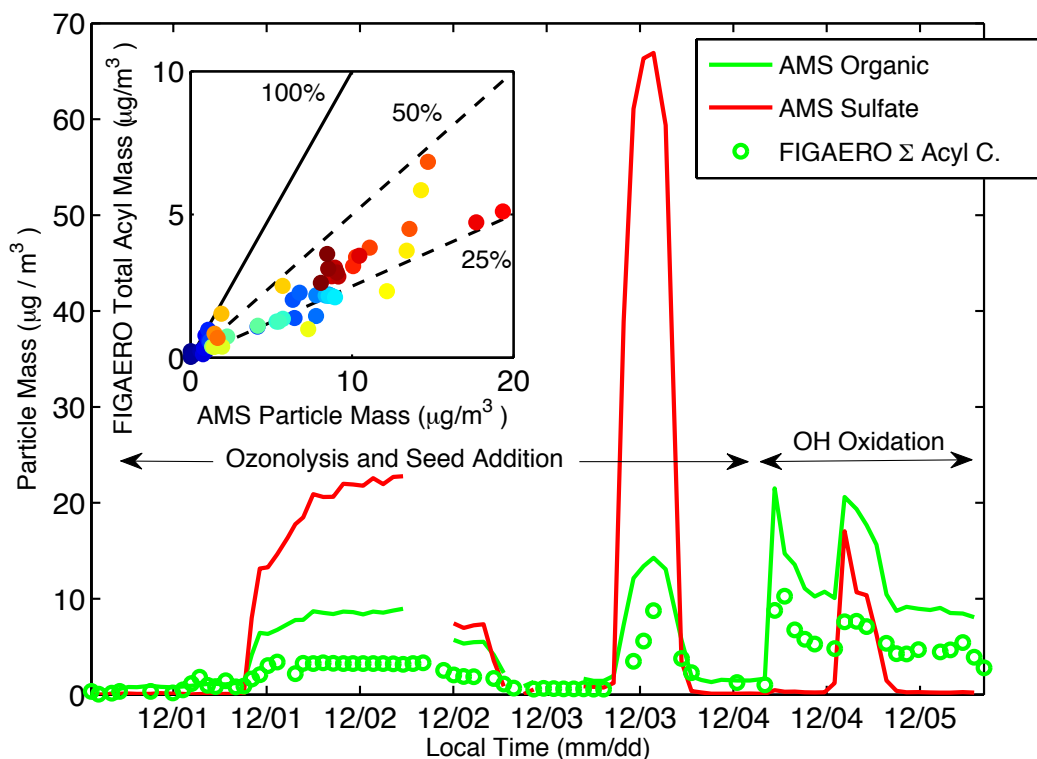
796

797

798

799

800

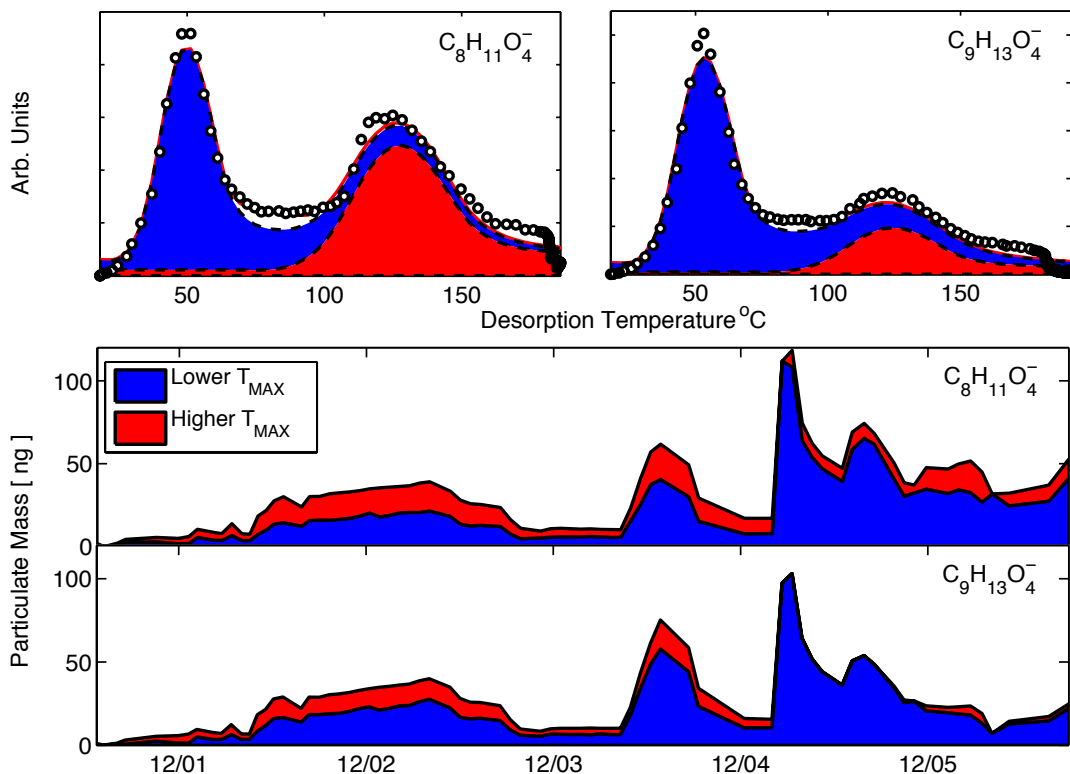


801

802 Figure 2. An overview of the experiments conducted in the JPAC chamber. Green and
 803 red lines are total organic and sulfate mass concentrations measured by an HR-AMS. The
 804 total organic aerosol mass detected by the AMS responded to changes in seed
 805 concentrations, increasing the inferred SOA yield. Size selected ammonium sulfate
 806 additions were performed to increase the particle surface area relative to chamber walls.
 807 The sum FIGAERO-HRTOF-CIMS particulate mass using acetate reagent ions is shown
 808 in green circles using the formic acid sensitivity for all detected compositions (see text
 809 for details). **Inset:** Correlation between the HR-AMS derived total organic aerosol mass
 810 concentrations and the FIGAERO HR-ToF-CIMS derived total “acyl” containing
 811 compound mass concentrations shows that across all chamber conditions the FIGAERO
 812 measurements explain 25-50% of the total organic aerosol mass.

813

814



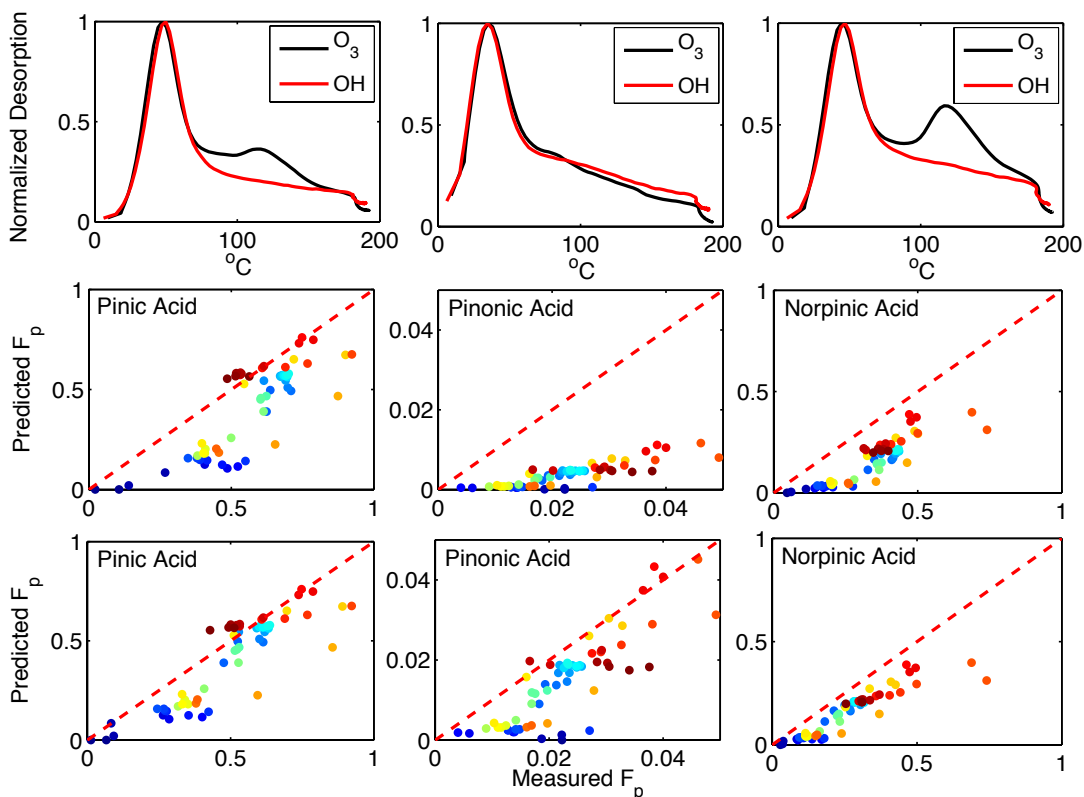
815

816 Figure 3. **Top panels:** Thermograms for two ion compositions, each showing two distinct
 817 modes in the thermogram, are plotted showing the results of fitting desorption profiles
 818 characteristic of an individual compound with a specific enthalpy of sublimation. The
 819 first, lower temperature, modes are consistent with the corresponding carboxylic acid
 820 desorbing as a non-interacting component of the collected organic aerosol. We attribute
 821 the second, higher temperature modes, to thermal decomposition of lower volatility
 822 compounds (such as oligomers or highly functionalized monomers) which are thermally
 823 unstable and which presumably do not affect the partitioning of the primary acids
 824 between the gas and particle phase. **Lower Panels:** The time series of the individual
 825 peak integrations within a fitted thermogram for the two different ion compositions
 826 across all chamber conditions. A significant fraction of the total detected signal arises
 827 from thermal decomposition (red) during desorption. Evident is the nearly complete
 828 disappearance of the second mode in $C_9H_{13}O_4^-$ (pinic acid) during OH oxidation
 829 suggesting that it is derived from a precursor that is only present during ozonolysis or
 830 which is reacted away in the presence of OH.

831

832

833

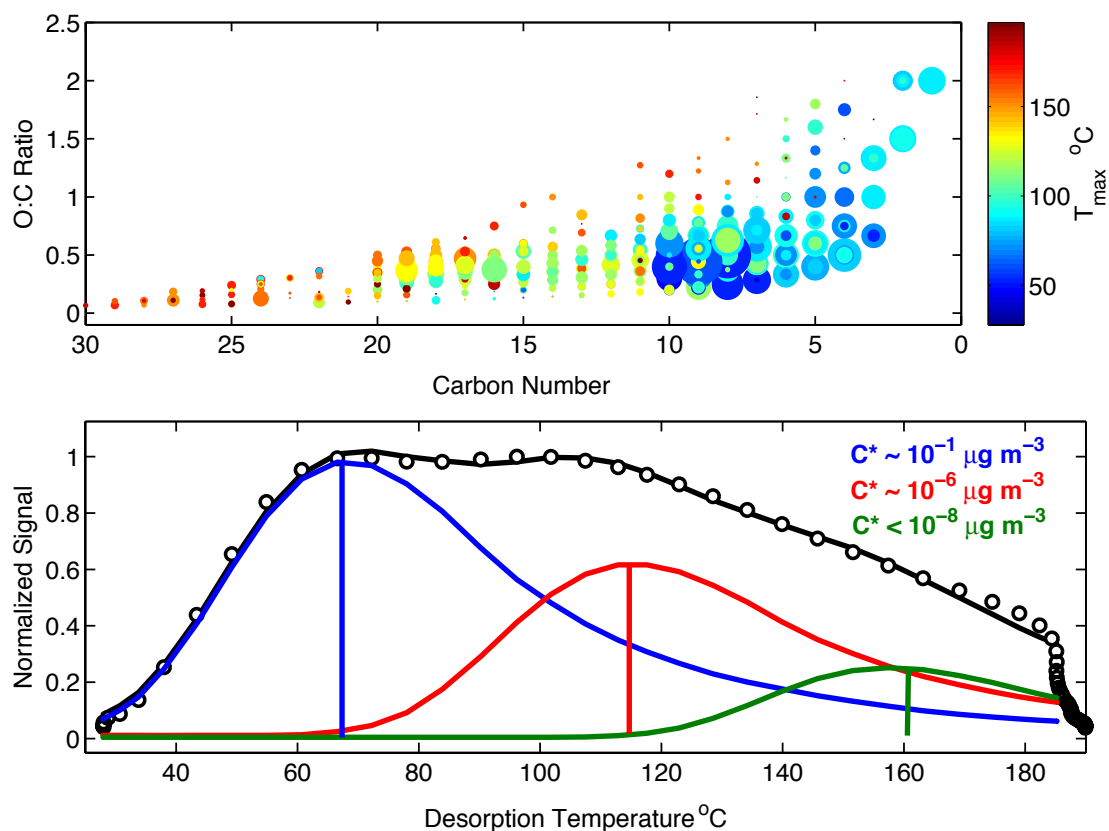


834

835 Figure 4. **Top panels:** Thermogram shapes for ozonolysis conditions (black) and OH
 836 oxidation (red) for the ion compositions corresponding to those of pinic, pinonic, and
 837 norpinic acids (left to right). **Middle panels:** Comparison between modeled and
 838 measured gas-particle partitioning (F_p). Generally poor agreement is found with non-
 839 linearity and points far from the 1:1 line (red dashed). **Bottom:** The same partitioning
 840 comparison but with the thermogram fitting routine (Figure 3) applied to remove the
 841 secondary modes in the desorption profile which are likely a result of thermal
 842 decomposition (see text for details). For pinonic acid a single desorption mode is
 843 observed under all conditions. To achieve model measurement agreement an activity
 844 coefficient of 0.25 is required, or the pure compound vapor pressure used is too high by a
 845 factor of ~ 4 .

846

847



848

849 Figure 5. **Top:** Points are plotted sized by the square root of their particle phase
 850 desorption signal. Evident is a secondary mode in abundance space between #C 15-20.
 851 Each compound is colored by the temperature of maximum desorption signal, which is
 852 related to a compound's enthalpy of sublimation (saturation vapor pressure) as shown
 853 previously (Lopez-Hilfiker, et al 2014). **Bottom:** A sum thermogram, i.e. the entire mass
 854 spectral signal at each measurement time (using selection criteria detailed in the text), is
 855 summed and plotted versus desorption temperature. Clearly SOA from α -pinene
 856 ozonolysis exhibits multiple modes. The first mode is consistent with monoterpene
 857 derived diacids, whereas the secondary modes which arise at temperatures >100 °C have
 858 effective vapor pressures at least 4 orders of magnitude lower than common monoterpene
 859 oxidation products.